A Test of Water Vapor Radiometer-Based Troposphere Calibration Using VLBI Observations on a 21-Kilometer Baseline

R. P. Linfield, L. P. Teitelbaum, and L. J. Skjerve
Tracking Systems and Applications Section

S. J. Keihm, S. J. Walter, and M. J. Mahoney
Microwave, Lidar, and Interferometer Technology Section

R. N. Treuhaft
Radar Science and Engineering Section

Simultaneous very long baseline interferometry (VLBI) and water vapor radiometer (WVR) measurements on a 21-km baseline showed that calibration by WVRs removed a significant fraction of the effect of tropospheric delay fluctuations for these experiments. From comparison of the residual delay variations within scans and between scans, the total tropospheric contribution to the delay residuals for each of the three 5- to 20-hour sessions was estimated as 1, 17, and 10 percent, with the first value being uncertain. The observed improvement in rms residual delay from WVR calibration during these three sessions was 4, 16, and 2 percent, respectively. The improvement is consistent with the estimated 2- to 3-mm path delay precision of current WVRs. The VLBI measurements, of natural radio sources, were conducted in April and May 1993 at Goldstone, California. Dual-frequency (2.3- and 8.4-GHz) observations were employed to remove the effects of charged particles from the data. Measurements with co-pointed WVRs, located within 50 m of the axis of each antenna, were performed to test the ability of the WVRs to calibrate line-of-sight path delays. Factors that made WVR performance assessment difficult included (1) the fact that the level of tropospheric fluctuations was smaller than is typical for Goldstone during these experiments and (2) VLBI delay variations on longer time scales (i.e., over multiple scans) contained uncalibrated instrumental effects (probably a result of slow temperature variations in the VLBI hardware) that were larger than the tropospheric effects.

I. Introduction

Ground-based observations at radio frequencies of compact natural radio sources or spacecraft can yield highly accurate position or velocity measurements. Very long baseline interferometry (VLBI) measures the relative delay in arrival time of wave fronts from a source at two or more sites. Spacecraft range

and Doppler tracking measure the delay, or its time derivative, of a round-trip radio signal transmitted between the ground and the spacecraft. In order to extract an angular position from a VLBI delay, a distance from a range measurement, or a radial velocity from a Doppler measurement, nongeometric components of the delay/delay rate must be removed. Many of these delay error sources can be estimated from VLBI data, provided that the functional form of the delay signatures of the error sources is known, and that these functional forms are significantly different from those induced by source angular position shifts. As an example, a clock offset and a linear (in time) clock rate can be estimated (and subtracted) from VLBI observations if multiple sources are observed or if one source is observed for an extended period of time.

The troposphere contributes approximately 7 ns of delay at the zenith, equivalent to a path length increase of $\Delta l_{zen} \approx 2.1$ m. (Hereafter, whenever a length is given for a delay, the delay in time units is that length divided by the speed of light.) At an elevation angle θ, the effective path length increase is $\approx \Delta l_{zen} / \sin \theta$. One can solve for the mean tropospheric zenith delay over some period of time by using a mapping function to relate the delay $\tau(\theta)$ at elevation angle θ to the zenith delay τ_{zen} ($\tau(\theta) = \tau_{zen} / \sin \theta$ is an approximate mapping function). Because of inhomogeneities in tropospheric refractivity, due primarily to inhomogeneities in water vapor density, estimating and subtracting such a mean troposphere will still leave a residual tropospheric delay that will corrupt the data.

The residual tropospheric delay was the largest error source in the astrometric VLBI observations of [1], where the authors were able to reduce the effects of the troposphere to ~1 cm on a 10,000-km baseline. This corresponds to an angular error of ~1 nanoradian (nrad), or 200 microarcseconds over angular scales of 30 deg on the sky. In order to achieve angular accuracies better than 1 nrad with VLBI, direct calibration of tropospheric delay is required. A sufficiently accurate line-of-sight delay calibration would enable substantial improvements in the accuracy of VLBI and spacecraft Doppler tracking measurements.

Because water vapor accounts for nearly all the small-scale structure in refractivity at microwave frequencies, efforts to calibrate line-of-sight delay have focused on measurements of water vapor. Water vapor radiometers (WVRs) measure thermal emission from water vapor at microwave frequencies. In order to test WVR wet delay calibration techniques, we designed and conducted a short-baseline VLBI experiment. By using a short baseline (21 km instead of the 3000- to 10,000-km baselines typically used for astrometric VLBI), many nontropospheric error sources were greatly reduced. Any geophysical modeling errors at each antenna cancel nearly perfectly over such a short baseline. Source position and Earth rotation/orientation errors result in very small delay errors. The short baseline allowed the use of the VLBI phase delay data type (described in Section IV), greatly reducing the thermal noise level. We expected tropospheric and instrumental (VLBI hardware) effects to be the two largest contributions to the measured residual delays.

II. Wet Troposphere Calibration

A. Wet Delay Formulation

The effect of the atmosphere on the propagation of a microwave signal, expressed as a range correction, or path delay τ, is the difference between the electrical and geometric path lengths:

$$\tau = \int_0^\infty (n - 1)ds = 10^{-6} \int_0^\infty N(s)ds \tag{1}$$

Here n is the refractive index, N is the refractivity, defined as the difference between the refractive index and unity, in parts per million, and the integrals are evaluated along the line-of-sight path through the atmosphere.

The refractivity is typically expressed as the sum of dry and wet (water vapor-induced) components [2], in which the dry component depends only on the density of dry air and the wet component depends on water vapor density ρ_v and physical temperature T. Using the formulation of [3], the wet refractivity component N_{wet} can be expressed as

$$N_{wet} = \left(K_1 \rho_v + K_2 \frac{\rho_v}{T} \right) Z_w^{-1} \qquad (2)$$

The Z_w, which accounts for nonideal gas behavior, has a value of 1.0 within 2×10^{-3} for atmospheric conditions [4]. Using the laboratory measurements of [5] for the constants K_1 and K_2, the wet delay τ_{wet} can be expressed as

$$\tau_{wet} = 10^{-6} \int_0^\infty \left(0.1095 \rho_v + 1733 \frac{\rho_v}{T} \right) ds \qquad (3)$$

Here ρ_v is in units of g/m^3, T is in kelvins, and τ_{wet} is in seconds.

Extensive evaluation [6] of the theoretical and experimental determinations of the vapor-induced refractivity component indicates that the relationship expressed in Eq. (3) is accurate at the 0.5-percent level. At microwave frequencies below 30 GHz, the wet refractivity component is practically nondispersive and the wet delay can be considered to be frequency independent.

B. WVR Measurements of the Wet Delay

Measurement of thermal emission from the optically thin 22-GHz water vapor spectral line is one potential method for calibrating the line-of-sight wet delay. A WVR measures sky brightness temperatures T_b at one or more frequencies near the 22-GHz peak, with an additional channel above 30 GHz to correct for emission from liquid water when clouds are present (e.g., [2]). Portable WVRs are steerable in both azimuth and elevation and typically have half-power beam widths (HPBW) of 6 to 9 deg.

WVR calibration is achieved by the use of an ambient reference target and tipping curves for system gain determination. During tip curve operations, WVRs obtain sky measurements over a range of elevation angles and utilize an extrapolation to zero air mass M ($M \equiv 1/\sin\theta$, where θ is the elevation angle) to establish the cosmic background temperature as the cold reference. The tip curve calibration method produces absolute brightness temperatures with accuracies <1 K and precisions <0.1 K for hour time scales. For periods during which tip curves are not available (e.g., during VLBI tracking), gain variations are estimated through their correlations with instrument temperatures. These correlations are established by one day or more of prior tip data.

The link between measured WVR brightness temperature T_b and atmospheric properties is provided by the standard microwave equation of radiative transfer for a nonscattering medium in local thermodynamic equilibrium [7]:

$$T_b = \int_0^\infty T(s)\alpha(\rho_v, T, P)e^{-\tau(s)}ds + T_{MB}e^{-\tau(\infty)} \qquad (4)$$

The optical depth, $\tau(s)$, is

$$\tau(s) = \int\limits_0^s \alpha(\rho_v, T, P) ds \qquad (5)$$

In Eqs. (4) and (5), $\alpha(\rho_v, T, P)$ is the volume absorption coefficient, including contributions from molecular oxygen, water vapor, and suspended cloud liquid (when present). The absorption depends upon the water vapor density ρ_v (and liquid density when clouds are present), the temperature T, and the pressure P, each of which in turn is a function of position along the line-of-sight path. The T_{MB} is the blackbody temperature of the cosmic microwave background radiation.

For clear-sky conditions, WVR brightness temperature T_b and the wet path delay τ_{wet} are highly correlated, because both are approximately proportional to the integrated water vapor content along the line of sight. This correlation has been demonstrated in a number of experiments that compared WVR-derived path delays to direct measurements with weather balloons [8,9] and inferred values from Global Positioning System (GPS) measurements [10,11].

Given a set of WVR brightness temperature measurements, the vapor-induced path delays are usually computed from a statistical retrieval (e.g., [12]). Atmospheric profiles measured by radiosonde flights at selected sites are used to generate a computational database of path delays and corresponding WVR brightness temperatures for a wide range of atmospheric conditions. Two or more years of twice-daily radiosonde profiles are typically used to characterize site conditions. A linear fit to the database produces an equation relating path delay to WVR brightness temperatures. For typical WVR measurement errors of 0.5 K, formal errors for retrieved zenith path delay of 2 to 3 mm are commonly obtained. This corresponds approximately to a 2- to 3-percent error for calibration of average ($\approx$10-cm) zenith wet path delays at sites used for spacecraft tracking. Other WVR wet path delay errors are described in Section II.C.

Independent wet delay calibration must be highly accurate in order to improve the accuracy of VLBI astrometric or spacecraft Doppler measurements. (Spacecraft range measurements are currently limited by calibration uncertainty in the delays through electronics, rather than by the troposphere.) VLBI astrometric measurements can be used to determine line-of-sight tropospheric delay to within $\approx$1 cm [1]. The line-of-sight wet delay for an elevation angle of 15 deg is typically 30 to 70 cm, so a calibration precision (if not accuracy) of $\sim$1 percent is needed in order to improve the accuracy of astrometric VLBI or Doppler data. A precision several times better than 1 percent is desired. Although WVRs have been tested against radio interferometric measurements previously [13],[1] wet delay calibration at the 1-percent level has never been demonstrated. The purpose of our observations was to find the limiting errors for such a demonstration.

C. Error Sources in WVR Measurements of Wet Path Delay

The 2- to 3-mm formal error in WVR-derived zenith wet delay stated in Section II.B includes only the effects of 0.5-K WVR "noise" and the variability of temperature and vapor height distribution. The formal error represents the rms accuracy that one would expect for WVR measurements with zero bias, a perfect absorption model, and a pencil beam. In applying WVR measurements as wet delay corrections for other instruments, a number of other error sources must be considered. Because our observations measured the difference in delay at the two sites, our sensitivity to some classes of WVR errors was reduced.

1. Unmonitored Gain Variations. WVR measurement errors are not properly characterized as pure noise with zero bias. The most serious instrumental uncertainty is due to unmonitored gain variations over time scales of minutes–hours, due primarily to temperature variations of the WVR electronic

---

[1] C. D. Edwards, "Water Vapor Radiometer Line-of-Sight Calibration Capabilities," JPL Interoffice Memorandum 335.1-90-015 (internal document), Jet Propulsion Laboratory, Pasadena, California, March 30, 1990.

components. For the WVRs used in this experiment, gain variations were monitored to the 0.05- to 0.1-percent level, either by estimating the gain from its strong correlation with mixer temperature measured during tip curve calibration or by time interpolation between tip curve data obtained before and after the VLBI observations. A 0.1-percent gain uncertainty corresponds to a 0.3-K WVR measurement error and a 1- to 2-mm uncertainty in the retrieved wet delay.

2. WVR Elevation Pointing Errors. WVR pointing errors can be significant at low elevation angles where brightness temperature varies most strongly with air mass. For the extremely dry conditions encountered at Goldstone during our observations, at 30 deg, the lowest WVR elevation angle employed, WVR brightness temperatures decreased by approximately 1 K for an elevation increase of 1 deg. For elevation uncertainties ~0.3 deg, typical of the Goldstone WVRs, the net effect on the wet delay retrieval error is ≤1 to 2 mm at a ≥30-deg elevation angle.

3. Vapor Absorption Model Error. The absolute uncertainty in any single measurement of WVR-derived wet delay is normally dominated by the 5-percent uncertainty [14] in the adopted vapor absorption model that links measured brightness temperatures to integrated vapor and path delay. For the dry Goldstone conditions, with average zenith wet delays of ~5 cm, this absolute error component is 2 to 3 mm. However, its effect was <1 mm, because the role of the WVRs in this VLBI experiment was to monitor the difference in delay between two sites, and the line-of-sight wet path delays at the two sites were similar.

4. Beam Offset and Mismatch Errors. The expected differences between wet delays sensed by WVR and DSN antennas depend on integration time, elevation angle, and the beam mismatch and beam axis offset between the instruments. For the Goldstone experiment, WVRs with conical 6- to 9-deg HPBW beams were deployed ≈50 m from the DSS-13 (26-m-diameter) and DSS-15 (34-m-diameter) antennas. Both of the DSN antennas have essentially cylindrical beams in the troposphere. Based on a turbulence model for the troposphere [15], the expected delay difference between the WVR and DSN beams for integration times >2 min and elevation angles >20 deg is <0.15 mm [16].

D. Additional Instrumentation

The formal or "inherent" WVR path delay retrieval error of 2 to 3 mm, described in Section II.B, is due primarily to variations of air temperature and water vapor density along the line of sight. To calibrate this error, additional instrumentation was deployed at Goldstone for the VLBI/WVR experiment. At DSS 15, a microwave temperature profiler (MTP) [17] was deployed. Using elevation-scanning measurements near the 60-GHz O_2 absorption band, the MTP provides atmospheric temperature profile data with accuracies of 1 to 2 K for altitudes below 3 km [18], where most of the water vapor resides.

In order to characterize the state of the atmosphere during the observations and to obtain independent site measurements of the vertical temperature and vapor density profiles, radiosondes were launched approximately every 6 hours. Our launch sites were 200 to 400 m from each antenna. Comparisons of the radiosonde measurements near the ground with measurements made by co-located surface sensors indicated that the radiosonde temperature and pressure measurements were accurate to 1 deg C and 3 mbar, respectively. However, similar comparisons revealed large and variable discrepancies in relative humidity measurements. We were thus unable to improve WVR path delay retrievals by constraining the relative height distribution of the vapor. The humidity sensors were a brand of carbon hygristors known to have problems at low humidity levels. Because of problems with the humidity sensors, we used the radiosonde data for only two purposes. First, the temperature profiles were used as validation for the MTP measurements of lower troposphere temperature profiles. Second, optical tracking of radiosonde flights at DSS 13 provided measurements of wind velocity and direction as a function of altitude. These measurements were used in modeling the magnitude of tropospheric turbulence effects on our VLBI data.

III. Observations and Data Reduction

A. VLBI

We conducted six VLBI observing sessions; their dates and durations are given in Table 1. We used two antennas of NASA's Deep Space Network in Goldstone, California: DSS 13 (26-m diameter) and DSS 15 (34-m diameter). The two antennas are separated by 21.3 km along azimuth 313 deg (DSS 15 is north and west of DSS 13).

Table 1. VLBI observing dates, 1993.

Session	Start day	Start UT	Duration, h
1	112	05:10	5.7
2	116	04:10	6.7
3	122	05:30	28.8
4	128	16:50	24.0
5	130	04:50	5.2
6	131	04:20	5.7

In addition, we observed with a 34-m-diameter antenna (DSS 65) in Madrid, Spain, during the first 24 h of session 3 and with a 34-m-diameter antenna (DSS 45) in Canberra, Australia, during all of session 4. Time on the DSS 15–DSS 65 baseline in session 3 and the DSS 15–DSS 45 baseline in session 4 had been previously allocated for astrometric VLBI observations. For these two sessions, we used the observing schedules created for those observations. These schedules were designed to provide geometric strength (i.e., allow the separation of baseline, source position, and tropospheric effects) on long baselines. The schedules emphasized two to four observations of each source, with each observation typically near rise, set, or transit at one of the two stations. Only results on the DSS 13–DSS 15 baseline are reported in this article.

For the other four 5- to 7-h sessions, our observing schedule was modified from an astrometric VLBI schedule to use stronger sources and have elevation angles >30 deg (thus allowing the co-pointing of WVRs, which cannot point below 30 deg without significant ground contamination of the measured brightness temperatures). In addition, we scheduled some long scans (300 to 700 s) on strong sources (typical scans were ≈150 s in length).

All VLBI observations used the Mk III recording system [19] in mode C, with five 2-MHz channels spanning 2200 to 2300 MHz (S-band) and nine 2-MHz channels spanning 8215 to 8583 MHz (X-band). Using two observing bands allows a calibration of the dispersive delay due to charged particles in the Earth's ionosphere and the interplanetary medium. (For an observing frequency ν well above the plasma frequency, the charged particle delay is proportional to ν^{-2}.)

After each 2-MHz channel was mixed to baseband, it was sampled at the Nyquist rate, digitized to 1 bit, and recorded on tape. In addition, the digitized data from DSS 15 were sent over optical fiber to DSS 13, where the DSS 13–DSS 15 baseline was correlated with the real-time Block II correlator [20]. The correlated data were written to disk for later processing. The results presented in this article are based upon data correlated in real time at DSS 13.

As a test of the accuracy of the real-time correlator, the data recorded on tape during session 5 were correlated with the JPL–CIT Block II correlator. The quality of tape playback was poor, and only 53 scans could be decoded. The difference between the S-/X-band group delays from the two correlators had a mean of 155 ps and a standard deviation of 3.5 ps. The mean delay offset is thought to be due to

details in the application of manual phase calibration in the observable extraction process (routine FIT) [21]. Because this offset looks exactly like a clock offset, it will not affect later results. The 3.5-ps rms is due at least in part to the poor quality of tape playback. However, even if it were due entirely to errors in the real-time correlator, it would be too small to significantly affect the results presented in Section V.

In order to calibrate the variation of instrumental delays with frequency and time, phase calibration was used at each antenna. Phase calibration tones were injected between the feed horn and the first stage RF amplifier, and later extracted by the correlator for use in correcting interferometric delays. At DSS 15, a phase calibration unit with a cable stabilizer [22] was used. This stabilizer greatly reduces the effect of path length changes between the hydrogen maser frequency standard on the ground and the tone generator at the feed horn. The entire system has an estimated error of ≤ 10 ps over 24 h due to diurnal temperature changes. Over time scales ≤ 6 h, the nonlinear delay errors were several times smaller than 10 ps. At DSS 13, the phase calibration unit did not have cable stabilization, and the instrumental delay calibration errors were, therefore, larger (this is discussed further in Section VI).

The postprocessing routine FIT was used to extract the residual phase from the correlated data for each scan, along with the derivatives of this phase with respect to frequency (group delay) and time (phase rate). The values of these quantities from the correlator model were added to the residual values to obtain total observables. The total phase produced in this way contained integer cycle ambiguities. These were resolved by a technique described in Section IV. When the integer cycle ambiguities were removed, the phase delay τ_{ph} could be calculated as $\tau_{ph} = \phi/\nu_{avg}$, where ϕ is the total phase at a mean observing frequency ν_{avg}.

B. WVRs

During each of the six VLBI sessions, WVRs were deployed near each of the two Goldstone antennas. A J-series WVR (J3) [23] was located 50-m north of the DSS-13 azimuth axis, and a D-series WVR (D2)[2] was located 40-m south of the DSS-15 azimuth axis. Both WVRs observed simultaneously in two channels, 20.7 and 31.4 GHz, with effective bandwidths of 320 MHz. The J3 instrument also has a 22.2-GHz channel (at the peak of the water vapor line), but this channel was not used during our observations. The estimated thermal noise level for 5- to 6-s integrations was approximately 0.06 K for D2 and 0.10 K for J3, corresponding to path delay errors of ≈ 0.4 mm (D2) and ≈ 0.6 mm (J3). Thermal WVR noise was not a limiting error source in this experiment.

During VLBI source measurements, the WVRs were co-pointed with the DSS-13 and DSS-15 antennas whenever viewing conditions allowed. However, unlike the two large radio antennas, the WVRs observed in a constant direction during a scan. Neither WVR was capable of taking data while slewing. The WVR 6- to 9-deg beams are subject to significant side lobe pickup whenever a substantial obstruction lies within ~ 20 deg of the beam axis. Prior to the experiment, the WVRs were operated in a horizon scanning mode to establish the azimuth-dependent minimum elevation angles free of ground pickup. For most observations and azimuths, 30 deg was chosen as a safe elevation angle lower limit. At DSS 15, where the D2 WVR sat on the ground to the south and substantially below the VLBI antenna, elevation angles <75 deg were precluded for source azimuths in the range (-45 deg, $+45$ deg).

While performing line-of-sight measurements during VLBI scans, both WVRs observed the sky nearly continuously, with 6-s interruptions once per minute to measure a reference load. The J3 WVR observed this load by internal switching, while the D2 unit slewed its antenna away from the radio source line of sight to an external ambient target. During gaps of 2 or more minutes between VLBI source measurements, the WVRs performed tip curves to monitor gain variations. For the J3 unit, the tip curves obtained during the VLBI observing gaps provided interpolation points for gain calibration during the 6-h sessions. For

---

[2] S. J. Keihm, *Water Vapor Radiometer Intercomparison Experiment: Platteville, Colorado, March 1–14, 1991*, JPL D-8898 (internal document), Jet Propulsion Laboratory, Pasadena, California, 1991.

the D2 unit, calibration variations were tracked using an empirical correlation between gain and mixer temperature established from tip curve data obtained prior to and following the VLBI observing sessions. The D2 tip curves obtained during gaps within the VLBI observing sessions provided a check on the precision of the mixer temperature gain tracking technique.

IV. Analysis

Data from the first three sessions were not usable for subsequent analysis. During session 1, instrumental phase calibration was not available at DSS 13. During session 2, hardware problems caused the loss of a large fraction of the VLBI data and most of the WVR data. During session 3, technical problems caused the instrumental phase calibration at DSS 13 to be too noisy to use. The number of usable scans, defined as having working phase calibration, adequate signal-to-noise ratio (SNR) for phase connection (discussed below), and valid WVR data from both DSS 13 and DSS 15, are given for all six sessions in Table 2.

Table 2. Quantity of usable data from each session.

Session	No. of usable scans
1	0
2	0
3	0
4	87
5	46
6	33

A. Calculating VLBI Phase Delays

The extraction of total VLBI delays for each scan at both S- and X-band was described in Section III.A. The one standard deviation (1σ) thermal noise $\Delta\tau_{SNR}$ in delay measurements, due to limited SNR in the data, is approximately

$$\Delta\tau_{SNR_g} \approx \frac{k}{2\pi\Delta\nu_{span}\,SNR} \qquad \text{for group delay} \tag{6}$$

$$\Delta\tau_{SNR_{ph}} \approx \frac{1}{2\pi\nu_{avg}\,SNR} \qquad \text{for phase delay} \tag{7}$$

The $\Delta\nu_{span}$ is the spanned bandwidth at X-band (368 MHz), and ν_{avg} is the mean X-band observing frequency (8405 MHz). The SNR is the signal-to-noise ratio for the entire scan, when all nine X-band frequency channels are combined. The k is a dimensionless factor that depends upon the spacing of channels over the spanned bandwidth. For channels stacked at the two band edges, $k = 2$. For uniform channel spacing, $k = 3\sqrt{2}$. For the spacings used during these observations, $k \approx 3$. The derivation of Eqs. (6) and (7) follows from the fact that, for thermal noise, the phase error (in radians) of a complex value is equal to the fractional amplitude error. Although the measured "charged-particle-free" delays are linear combinations of S- and X-band delays, the errors are dominated by the X-band delay errors because the X-band delay weights in the linear combination are a factor of $(\nu_X/\nu_S)^2 \approx 14$ times larger than the S-band weights.

The values of $\Delta\tau_{SNR_g}$ ranged from <1 ps to >30 ps, with $\Delta\tau_{SNR_g} \geq 10$ ps for many scans. Because the goal of this experiment was to look for mm-level effects (1 mm corresponds to ≈ 3 ps), we used the phase delay observable τ_{ph}:

$$\tau_{ph} \equiv \frac{\phi}{\nu_{avg}}$$

Here ϕ is the total phase in cycles, including integer cycles, at the mean X-band frequency ν_{avg}. Use of the phase delay reduced $\Delta\tau_{SNR}$ a factor of ≈ 20 below that for the group delay.

The group delays were used to resolve integer cycle ambiguities (i.e., to "connect phase" from one scan to the next) in the phase delays. In order for this to be accomplished, the thermal noise in the group delays had to be sufficiently small that the probability of making a cycle error was negligible. If we set a 5-σ threshold for a cycle error (defined as an error in the group delay of >0.5 cycle), then

$$\Delta\tau_{SNR_g} < \frac{0.1}{\nu_{avg}}$$

This leads to

$$SNR > \frac{10k\nu_{avg}}{2\pi\Delta\nu_{span}} \approx \frac{30\nu_{avg}}{2\pi\Delta\nu_{span}}$$

For S- and X-band, the constraints on SNR are

$$SNR_S > 110$$

$$SNR_X > 110$$

Because charged particles affect group and phase delays with opposite signs, it was not possible to perform phase connection using raw delays. The following procedure was used. First, the S- and X-band group delays were used to derive a charged-particle-free group delay, $\tau_g(S/X)$, and an electron column density, N_g. The accuracy of both quantities was limited by thermal noise in the group delays. Second, N_g was used to remove most of the charged-particle contribution to the S- and X-band phase delays. Using $\tau_g(S/X)$, the integer cycle ambiguities in these phase delays were determined. The corrected phase delays were then used to estimate very high SNR charged-particle-free phase delays, $\tau_{ph}(S/X)$, which were used for subsequent analysis. This procedure could also have used the phase delays to determine the electron column density with high precision, but this quantity was not needed for the analysis in this experiment.

B. VLBI Parameter Estimation

The charged-particle-free phase delays for each observing session were analyzed using JPL's program MODEST (for model and estimation) [24]. First, an a priori model delay was subtracted from each scan. This model included atmospheric, source, baseline, relativistic, and geophysical parameters. For the short baseline in this experiment, many components of this model gave a negligible contribution. The dominant components of the model consisted of (1) a geometric term, based on UT1 (i.e., universal time corrected for Earth rotation irregularities UT1−UTC), station locations for the two antennas, and source positions converted from J2000 to date via precession, nutation, and aberration, and (2) a media term,

consisting of tropospheric delay differences. The a priori differential dry zenith delays were derived from surface pressures at the two antennas and the elevation angles of the sources. For our a priori model of wet delay differences, we used either zero (i.e., no calibration) or the station-differenced line-of-sight WVR wet path delay estimates. Both options were used for all sessions so that the effectiveness of WVR calibration could be quantified.

The model subtraction produced a set of residual delays. The estimation process did an unweighted least-squares fit to these residuals, solving for one or more parameters. Equal weighting was used because the thermal noise was much less than other error sources (tropospheric fluctuations and instrumental effects). In all cases, a constant clock offset was estimated. Other parameters estimated during some runs were a residual mean zenith troposphere difference and a correction to the baseline vector between the two antennas.

The clocks at the two antennas were derived from the same frequency standard. However, the cable lengths distributing this standard to the two antennas were different, so that the mean differenced clock value at the two antennas was nonzero. This parameter reduced the rms scatter among the residuals (i.e., the interscan residuals) to <30 ps for sessions 5 and 6 and ≈80 ps for session 4.

The residual mean zenith-troposphere difference parameter primarily represented the session-averaged difference in the wet delays (DSS 15 consistently had a larger wet delay than DSS 13). However, it also accounted for any calibration error in the dry delay difference between the two sites.

For session 4, when there were a large number of scans with broad sky coverage, an attempt was made to solve for a correction to the vector baseline between the two antennas. However, solving for these additional three parameters resulted in minimal reduction to the interscan residuals. For all results reported below, the baseline was left unchanged from its a priori value, derived from multiple previous VLBI observations.

Because most or all VLBI astrometric and geodetic results have been based on group delays, we checked for possible systematic errors in the calculation and treatment of phase delays. Group delays were used in comparison runs of MODEST for sessions 5 and 6, both with and without WVR calibration. The resulting VLBI interscan group delay rms values were equal, in all cases, to the residual phase delay rms values with ≈10 ps of noise added in quadrature. We conclude that any systematic errors in the phase delays were substantially less than 10 ps.

C. WVR-Based Delay Residuals

Site-differenced line-of-sight wet delays were determined from the WVR data at ≈6-s intervals for each VLBI source observation. The two-channel line-of-sight WVR brightness temperatures were first converted to zenith-equivalent brightness temperatures using the effective radiating temperature approximation to Eq. (4) in [2]:

$$T_b(M) = T_{eff} - (T_{eff} - T_{MB}) e^{-\tau(M)} \qquad (8)$$

The value of T_{eff} used was 285 K. The T_{MB} is the cosmic background microwave temperature, and M is the air mass ($M \equiv 1/\sin\theta$, where θ is the elevation angle). Given a value for $T_b(1)$ (i.e., T_b at the zenith), $\tau(1)$ can be computed and the path delay can be accurately mapped to any other elevation angle >15 deg using the relation $\tau(M) = \tau(1)/\sin\theta$.

Once converted to zenith, the WVR brightness temperatures were used to determine zenith path delay. A linear retrieval algorithm was based on correlations between Desert Rock, Nevada, radiosonde measurements of zenith path delay and computed WVR brightness temperatures. The brightness temperatures were generated from the radiosonde data using the modified Liebe vapor absorption model [14].

Desert Rock is considered the site equivalent of Goldstone, both in altitude and average moisture content. The path delay retrieval algorithm generates three path delay values for each input set of WVR zenith brightness temperatures: one using both channels and one each using the channels independently. For most operating conditions, the two-channel algorithm provides the most accurate path delay results. For time intervals under cloudless conditions for which the behavior of one channel is anomalous or subject to larger than normal gain uncertainties, the single-channel algorithms can be applied using data from the more reliable channel. Other algorithms, which augmented the WVR data with MTP measurements of the lower troposphere temperature profile, were also tried, but produced no additional reduction in the final VLBI site-differenced residuals.

When the WVR data were included in the VLBI processing, the derived zenith WVR delays were mapped to the DSN antenna elevation for each pass. If no obstructions precluded co-pointing, the mapping coincided with the original WVR pointing. These data are considered the highest-quality WVR measurements of path delay correction and were assigned a quality flag of 3. If co-pointing did not occur but the WVR and VLBI antennas were aligned within one WVR HPBW (7 deg), then a quality flag of 2 was assigned. If there was some indication of WVR ground pickup of magnitude <1 K, then a quality flag of 1 was assigned. With evidence of ground pickup exceeding 1 K or any indication of anomalous WVR calibration behavior, the quality flag was set to 0. For all results reported in the following section, only quality flag ≥2 data were utilized. These data comprised ≈70 percent of the passes of VLBI observation sessions 4, 5, and 6.

V. Results

A. Interscan Delay Residuals

The results of the MODEST runs for sessions 4 through 6 are summarized in Tables 3 and 4. Results without VLBI troposphere estimation are listed in Table 3; results with VLBI troposphere estimation are listed in Table 4. All entries in these tables correspond to VLBI scan-averaged phase delay residuals. Column 3 in each table gives rms VLBI interscan post-fit delay residuals when WVR line-of-sight wet path delay estimates were applied as calibration. These estimates use two-channel (20.7- and 31.4-GHz) retrievals for the J-WVR and one-channel (31.4-GHz) retrievals for the D-WVR. Other combinations were also tried but gave inferior results. As discussed below, the D2 channel-1 data were apparently corrupted by instrument pointing problems. The WVR calibrations reduced the post-fit residuals for all three sessions.

Table 3. VLBI interscan rms residuals without mean zenith troposphere estimate.

Session	No WVR calibration, ps	Dual channel for J3, channel 2 for D2, ps
4	80.0	77.2
5	22.6	16.3
6	24.2	23.3

The VLBI scan-averaged residual phase delays (i.e., after the least-squares fits in MODEST) and WVR station-differenced path delays for sessions 5 and 6 are shown in Fig. 1. The MODEST VLBI solution used for this figure included the estimation and subtraction of a mean tropospheric zenith delay but did not include WVR calibration. The line-of-sight residual delays (one for each scan) have all been mapped to the zenith, using the factor $\sin \theta$, where θ is elevation angle. The mean zenith delay has been removed from the WVR delays. This process allows a more valid comparison with the VLBI residual delays,

Table 4. VLBI interscan rms residuals with mean zenith troposphere estimate.

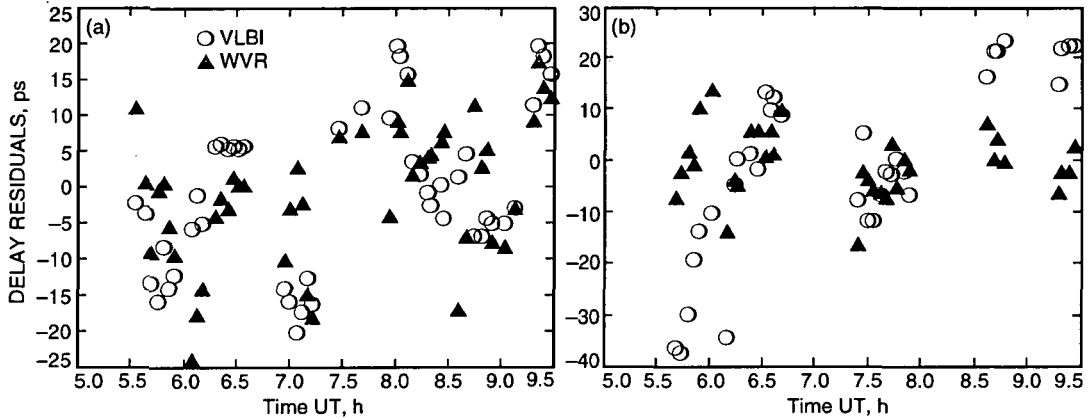| Session	No WVR calibration, ps	Dual channel for J3, channel 2 for D2, ps
4	80.0	77.2
5	14.4	12.1
6	23.5	23.0

Fig. 1. VLBI interscan phase delay residuals and WVR delay estimates: (a) session 5 and (b) session 6. A mean tropospheric zenith delay has been subtracted from both the VLBI and the WVR data. A constant delay (clock offset) has been subtracted from the VLBI data.

which have also had a linear delay fitted and subtracted. Examination of Fig. 1 shows good correlation between the VLBI and WVR delay changes during some limited time intervals. However, there are large systematic differences at other times. In order to understand those differences, we examined the VLBI and WVR delay variations in several ways.

The standard deviations of the zenith residuals for VLBI and for single-site and site-differenced WVR zenith delays are given in Table 5. The VLBI values correspond to those plotted in Figs. 1(a) and 1(b): line-of-sight values with a clock and mean zenith troposphere removed, and the delays then mapped to zenith. The WVR values had a constant offset removed from the zenith delay values. As in Tables 3 and 4, the WVR results for D2 are based on channel 2 only. If the VLBI interscan residuals were dominated by the troposphere, we would expect the WVR site-differenced residuals to be at least as large as the VLBI residuals (equal if the WVR measurement errors were much smaller than the troposphere, and larger otherwise). The scatter in the site-differenced WVR delays was significantly less than in the VLBI delays for session 5 and especially for session 6. Over the duration of a session, either the WVRs underestimated the tropospheric variations or the VLBI measurements had some significant noise source in addition to the troposphere.

Because the sites at DSS 13 and DSS 15 were nearby and similar, we would expect the individual-site WVR standard deviations to be comparable. The fact that the D2 residual rms values were substantially larger than the J3 residuals suggests that D2 instrument errors contributed significantly to the D2 residuals. The mechanical design of the D-WVRs makes them more susceptible to pointing errors than J-WVRs. An elevation angle offset for each D2 channel was estimated from tip curves: 0.9 deg for channel 1 and 0.5 deg for channel 2. However, because all tip curves during our observations were performed along one azimuth, there was no way to determine the azimuth dependence of these offsets. With an unknown azimuth dependence for both channels, the pointing error for channel 1 was expected

Table 5. VLBI and WVR interscan rms zenith delay residuals.

Session	VLBI, ps	WVR: site differenced, ps	J3, ps	D2, ps
5	10.7	9.5	7.0	8.7
6	10.3	6.4	7.4	10.0

to be larger than for channel 2. An elevation error of 0.5 deg in channel 2 at a 30-deg elevation angle would cause a fractional error of 2 percent, or ≈6 ps for the conditions during these observations.

B. Intrascan Delay Variability

In order to analyze the delay variations on short ($\leq$700-s) time scales, we calculated structure functions from WVR line-of-sight delays and from residual VLBI phase delays within individual scans (i.e., intrascan residuals). For a delay τ measured at time t, the structure function $D_\tau(\Delta t)$ for a time interval Δt is $D_\tau(\Delta t) \equiv \left\langle [\tau(t) - \tau(t + \Delta t)]^2 \right\rangle$. We used long ($\geq$300-s) scans in this comparison, because these scans provided the largest possible logarithmic range of time interval.

For each of sessions 5 and 6, WVR structure functions (using individual 5- to 6-s integrations) were calculated for all long scans, mapped to a reference elevation angle (described below), and averaged. There were four such scans in session 5 and thirteen in session 6. The mapping between elevation angles (for both WVR and VLBI structure functions) was determined from numerical integration of the Treuhaft–Lanyi model; it was $\approx \sin\theta_{obs} / \sin\theta_{ref}$, where θ_{obs} is the elevation angle where the structure function was measured and θ_{ref} is the reference elevation angle. The averaged structure function for each WVR was then multiplied by 2, because each was derived from single-station data and the VLBI structure functions were derived from station-differenced data.

All long scans in sessions 5 and 6 had VLBI elevation angles θ_{VLBI} >37 deg or <20 deg. For VLBI structure functions, the low elevation angle (<20 deg) scans could not be used. At these low elevation angles, sidereal tracking causes a significant nonlinear air mass change with time. Combined with imperfectly modeled zenith delays (i.e., the static troposphere), this effect corrupted the measurement of actual fluctuations. (Because the WVRs did not move during observations, their structure functions did not suffer from this problem.) The structure functions (based on residual $\tau_{ph}(S/X)$ values for 2-s integrations) from all long scans with θ_{VLBI} > 37 deg (three in session 5 and one in session 6) were mapped to θ_{ref} and averaged. The reference elevation angle θ_{ref} was the mean VLBI elevation angle for these scans in each session (θ_{ref} = 38.5 deg in session 5 and θ_{ref} = 40.3 deg in session 6).

The WVR and VLBI structure functions are shown in Fig. 2(a) for session 5 and Fig. 2(b) for session 6. In Fig. 2(a), the curve labeled "VLBI (AVG)" is the average of the VLBI structure functions for the three long ($\geq$ 600-s) scans at elevation angles >30 deg. The curves labeled "J3 (AVG)" and "D2 (AVG)" are the averages of the J3 and D2 WVR structure functions for all four long scans. All structure functions have been scaled to a constant elevation angle, 38.5 deg, before averaging. The WVR structure functions have been multiplied by 2 for comparison with the two-station VLBI structure functions. At time scales less than ~100 s, the WVR structure functions (especially for J3) are dominated by thermal noise. The VLBI structure function is not shown for time scales >300 s, because the least-squares delay rate fitting performed on the data (by FIT) has suppressed the structure function in this regime. For session 6, Fig. 2(b), there was only one long VLBI scan at elevation angle >30 deg, and 13 WVR scans. The WVR structure functions were mapped to the VLBI elevation angle of 40.3 deg before averaging. Because only one WVR scan was longer than 300 s, the WVR structure functions are only shown for 0 to 300 s. Except at time scales <100 s, where thermal noise dominates the WVR structure functions, the VLBI and WVR structure functions in Fig. 2 show a qualitative agreement.
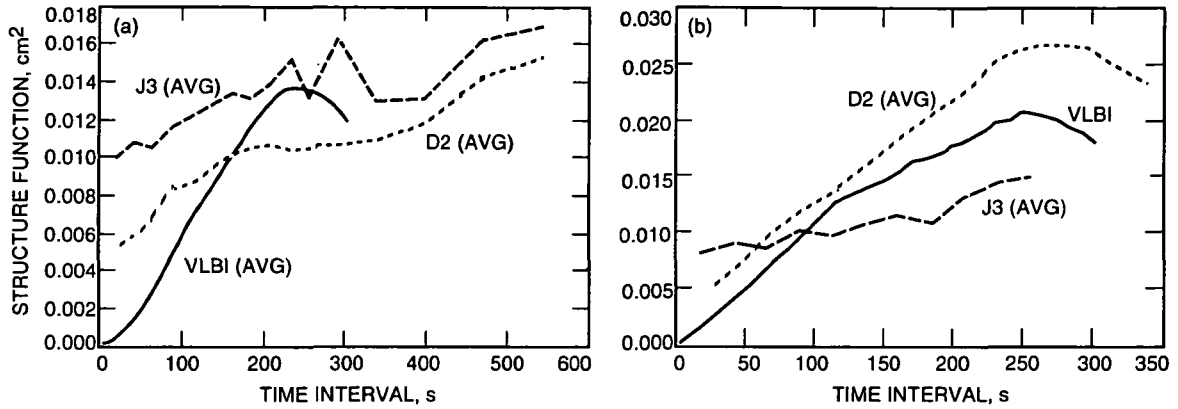
Fig. 2. VLBI and WVR intrascan structure functions, shown on a linear scale: (a) session 5 and (b) session 6.
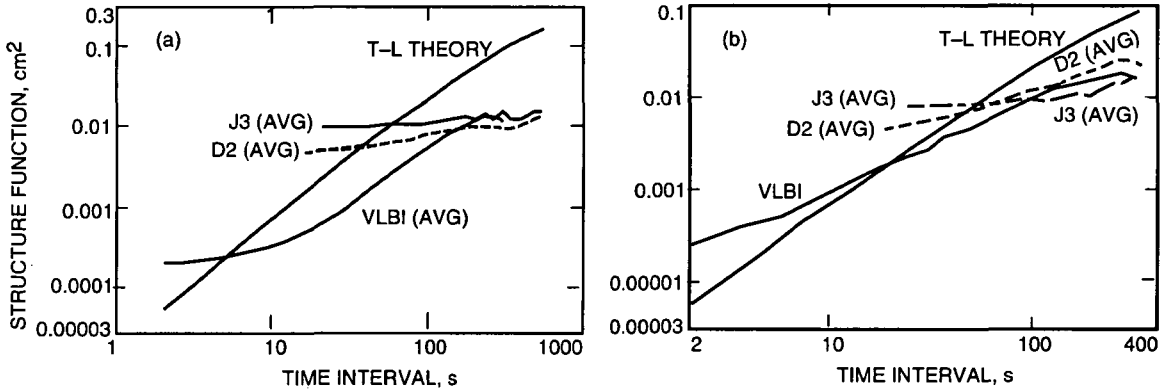

Fig. 3. VLBI and WVR structure functions shown on a log scale: (a) session 5 and (b) session 6. The theoretical Treuhaft–Lanyi structure function for average Goldstone tropospheric conditions ($C\chi = 7 \times 10^{-8}$ $m^{-1/3}$) is shown for comparison. The VLBI structure function is dominated by thermal noise on time scales less than ~10 s.

In Figs. 3(a) and 3(b), the VLBI and WVR structure functions are shown on a logarithmic scale. Also shown for comparison is the theoretical Treuhaft–Lanyi structure function for θ_{ref} under typical Goldstone conditions ($C_\chi = 7 \times 10^{-8}$ $m^{-1/3}$, the mean Goldstone value derived from intercontinental DSN VLBI observations, 8 m/s wind velocity). The thermal noise floor in both the WVR and VLBI structure functions can clearly be seen. At time scales >100 s (i.e., where thermal noise is not important), the measured structure functions (for both VLBI and WVRs) are a factor of 2 to 4 smaller than expected for normal conditions.

C. Session Average VLBI Structure Functions

In order to quantify the average level of tropospheric activity for each session, high SNR scans were used to determine the VLBI structure function. The measured VLBI D_τ values were compared to theoretical structure functions, based upon the model of [15], and the results are presented in Table 6. The parameters in the model include elevation angle (chosen to be the same as in the individual VLBI scans), vector wind velocity, tropospheric slab height (chosen to be 2 km, the mean wet tropospheric scale height), and the structure constant C_χ (7×10^{-8} $m^{-1/3}$). Vector wind velocities as a function of height were measured by optical tracking of our radiosondes at DSS 13, with launches every 6 hours. The vector wind velocities used in the structure function calculations were linear interpolations (in time) of the values measured by radiosonde tracking.

Table 6. Measured and theoretical delay structure functions.

Session	Scan	Δt used for D_τ, s	$\sqrt{\dfrac{D_\tau (measured)}{D_\tau (theory)}}$	Mean value	Predicted interscan line-of-sight rms residual, ps
4	11	16	0.48		
	35	16	0.80		
	145	16	0.54		
	160	16	0.40		
	199	16	0.16		
	212	16	0.29		
	237	16	0.17		
	276	16	0.23		
	309	16	0.28		
				0.37	9.7
5	2	50	0.32		
	12	16	0.26		
	27	16	0.30		
	33	50	0.27		
	40	16	0.48		
	60	16	0.51		
	65	50	0.32		
				0.35	8.1
6	4	50	0.48		
	8	16	0.34		
	20	16	0.48		
	35	16	0.37		
	38	50	0.95		
	54	16	0.34		
	59	50	0.20		
				0.45	10.2

For each scan, the square root of the ratio of measured to theoretical value of D_τ is given in column 4 of Table 6. The value of Δt used to determine this ratio was 50 s for 700- to 800-s scans and 16 s for 100- to 150-s scans, as indicated in column 3. These Δt values were chosen to be large enough to yield negligible contribution from thermal noise, yet short enough that D_τ was not significantly reduced by the linear delay rate subtraction done by FIT. The quantity in column 4 varies linearly with C_χ. Column 5 gives the mean of the column 4 values for each session. As was evident from Figs. 3(a) and 3(b), the magnitude of water vapor fluctuations during this experiment was significantly less than normal for Goldstone.

For each session, a corrected value of C_χ was obtained by multiplying the nominal value $(7 \times 10^{-8} \text{ m}^{-1/3})$ by the mean $\sqrt{D_\tau (measured)/D_\tau (theory)}$ value. The corrected C_χ value represented the mean tropospheric activity, as measured from the intrascan residuals. This C_χ value was used to calculate the tropospheric delay standard deviation $\sigma(T)$ expected for the entire session (i.e., the interscan rms residual). The variance $\sigma^2(T)$ of a random process over an interval T can be expressed in terms of the structure function as [15]

$$\sigma^2(T) = \frac{1}{T^2} \int\limits_0^T (T - t) D_{\tau_{2stn}}(t) dt \qquad (9)$$

In Eq. (9), $D_{\tau_{2stn}}(t)$ is the two-station delay structure function, the expected square of the line-of-sight delay difference at the two sites (DSS 13 and DSS 15). Using a frozen flow model, separations in space and time are related through the vector wind velocity $\vec{v}_w$. Thus, for a time interval Δt, the vector used for the calculations of $D_{\tau_{2stn}}(t)$ is $\vec{v}_w \Delta t + (\vec{x}_{15} - \vec{x}_{13})$, where $\vec{x}_{15}$ and $\vec{x}_{13}$ are the locations of DSS 15 and DSS 13. For time scales much less than the wind crossing time of the interferometer (i.e., $\Delta t << \|\vec{x}_{15} - \vec{x}_{13}\|/v_w$), variations at the two sites are uncorrelated, and $D_{\tau_{2stn}}(t) \approx 2D_{\tau_{1stn}}(t)$, where $D_{\tau_{1stn}}(t)$ is the single-station delay structure function. This approximation was used for the calculations in Sections V.A and V.B. The time scale used in evaluating Eq. (9) was the length of a session, and the wind velocity was the mean value measured at a 1-km height during that session. Because the scans in each session had a reasonably uniform distribution over any one quadrant of the sky, a source-wind azimuth of 45 deg was used in these calculations. The dependence of calculated tropospheric effects upon wind velocity is fairly weak. Use of the default wind velocity of 8 m/s changed the estimated tropospheric interscan rms by <20 percent. For the elevation angle in the model, we used the mean air mass-weighted elevation angle for all VLBI scans in a session that had high-quality WVR data at both stations: 42 deg for session 4, 47 deg for session 5, and 50 deg for session 6. The results of these calculations are given in column 6 of Table 6.

D. Implications of the Model Predictions of Interscan VLBI Residuals

A comparison of VLBI-measured and the model-predicted interscan residuals is given in Table 7. For each session, the predicted delay rms due to the troposphere, based on the VLBI intrascan structure functions (column 6 of Table 6), is shown in column 2. The measured VLBI rms, with a solution for a mean troposphere but without WVR calibration (column 2 of Table 4), is given in column 3. The discrepancy between the values in columns 2 and 3 indicates that nontropospheric (i.e., instrumental) errors were the major source of the VLBI interscan delay residuals.

Table 7. Comparison of expected and actual VLBI residual delay improvement from WVR calibration.

Session	Predicted tropospheric interscan rms, ps	Actual VLBI rms, ps	Expected rms reduction from perfect tropospheric calibration, %	Actual rms reduction from WVR calibration, %
4	9.7	80.0	1	4
5	8.1	14.4	17	16
6	10.2	23.5	10	2

Significant instrumental delay variations at DSS 13 could have remained uncalibrated. Table 8 gives the rms phase delay variation (with respect to a least-squares linear fit in time) for the instrumental phase calibration measurements at each station for sessions 4 through 6, at both S- and X-band. The instrumental delay variations at DSS 13 were significantly larger than for DSS 15 during all three sessions. If the phase calibration had worked perfectly, even the larger DSS-13 variations would not pose a problem. However, the DSS-13 phase calibration system was not able to measure delay changes on the transmission from the control room up to the antenna focus. We suspect that these instrumental delay changes constituted the nontropospheric component of our interscan rms. Instrumental delay changes due to mechanical motion of the antenna would likely be much smaller during sidereal tracking than when the

antenna slewed from one source to another. Instrumental changes due to thermal variations are likely to be important only over time scales longer than approximately an hour, when significant temperature changes can accumulate.

**Table 8. RMS phase delays (one delay per scan)
from phase calibration.**

Session	DSS-13 S-band, ps	DSS-13 X-band, ps	DSS-15 S-band, ps	DSS-15 X-band, ps
4	181	167	8	9
5	10	11	4	4
6	29	30	7	4

As a further test of the nature of the VLBI residuals, their elevation angle dependence was examined. For the case where WVR calibration was not applied, the VLBI residuals for some low elevation angle scans were large. When there was a long antenna slew after several scans in a small area of the sky, there was often a substantial change in the residuals. Both of these effects went away when WVR calibration was applied, suggesting that tropospheric effects (largest at low elevation angles or when comparing two regions that are far apart on the sky) had been largely removed. The signature of the VLBI residuals *with* WVR calibration was a systematic variation on time scales >1 h, with no obvious elevation angle dependence. We suspect that thermal variations in the DSS-13 antenna or receiver system were the most likely cause of the largest component of the long-term (interscan) residuals.

If the troposphere model calculations are correct, perfect line-of-sight tropospheric delay calibrations would reduce (in quadrature) the total rms (column 3 in Table 7) by the amount in column 2. This "perfect calibration" interscan rms improvement, Δ_{cal}, is given in column 4.

$$\Delta_{cal} \equiv 1 - \sqrt{\frac{\sigma_{VLBI}^2 - \sigma_{Trop}^2}{\sigma_{VLBI}^2}}$$

Here the total rms and the tropospheric rms are represented by σ_{VLBI} and σ_{Trop}, respectively. The measured improvement from WVR calibration (derived from values in Table 4) is given in column 5 of Table 7. Except for session 6, the improvement from WVR calibration is a large fraction of the calculated maximum improvement. This shows that WVR measurements were able to calibrate the majority of the wet tropospheric fluctuations.

VI. Conclusions

Application of WVR calibration resulted in a definite but minor (2- to 16-percent) reduction in the VLBI interscan rms residual delays and is consistent with our understanding of the relative amounts of instrumental and atmospheric fluctuations. We conclude that, over the duration of an observing session, the VLBI residual delays had a larger instrumental component than a tropospheric component, and that the WVR calibration removed most of the tropospheric component of these delays. This conclusion is based upon the following evidence:

(1) Within scans, the WVRs and VLBI measured similar levels of delay variations (intrascan residuals), as shown by the agreement in their structure functions (Figs. 2 and 3). On longer time scales, the VLBI delay residuals were larger than the WVR residuals (Table 5).

(2) The VLBI residual values *within* and *between* scans are not consistent. The level of intrascan residuals implies that the interscan residuals should be a factor of 1.8 to 8 smaller than was actually measured. This is most easily explained by a nontropospheric component to the long time-scale VLBI residuals.

(3) WVR calibration of VLBI delays reduced the interscan residuals for all three sessions. For sessions 4 and 5, the reduction was nearly equal to the amount calculated as being due to the troposphere.

(4) The WVR site-differenced zenith rms delays were substantially smaller than the VLBI residual rms delay.

Our test of the wet delay calibration ability of WVRs was hindered by the quiet nature of the troposphere during these observations. Future tests should be conducted during times (e.g., summer afternoons) when convection-driven atmospheric turbulence is common.

Acknowledgments

References

[1] R. N. Treuhaft and S. T. Lowe, "A Measurement of Planetary Relativistic Deflection," *The Astronomical Journal*, vol. 102, no. 5, pp. 1879–1888, November 1991.

[2] G. Elgered, "Tropospheric Radio Path Delay From Ground-Based Microwave Radiometry," Chapter 5, *Atmospheric Remote Sensing by Microwave Radiometry*, edited by M. Janssen, New York: Wiley & Sons, 1993.

[3] G. D. Thayer, "An Improved Equation for the Radio Refractive Index of Air," *Radio Science*, vol. 9, no. 10, pp. 803–807, October 1974.

[4] J. C. Owens, "Optical Refractive Index of Air: Dependence on Pressure, Temperature, and Composition," *Applied Optics*, vol. 6, pp. 51–58, 1967.

[5] G. Boudouris, "On the Index of Refraction of Air, the Absorption and Dispersion of Centimeter Waves by Gases," *J. Res. Natl. Bur. Stand., Sect. D*, vol. 69D, no. 6, pp. 631–684, 1963.

[6] R. J. Hill, R. S. Lawrence, and J. T. Priestly, "Theoretical and Calculational Aspects of the Radio Refractive Index of Water Vapor," *Radio Science*, vol. 17, no. 5, pp. 1251–1257, September–October 1982.

[7] S. Chandrasekhar, *Radiative Transfer*, Chicago: University of Chicago Press, 1950.

[8] E. R. Westwater, J. B. Snider, and M. J. Falls, "Ground-Based Radiometric Observations of Atmospheric Emission and Attenuation at 20.6, 31.65, and 90.0 GHz—A Comparison of Measurements and Theory," *IEEE Trans. Antennas Propag.*, vol. 38, no. 10, pp. 1569–1580, October 1990.

[9] M. N. England, F. J. Schmidlin, and M. M. Johansson, "Atmospheric Moisture Measurements: A Microwave Radiometer—Radiosonde Comparison," *IEEE Trans. Geoscience and Remote Sensing*, vol. 31, no. 2, pp. 389–398, March 1993.

[10] S. M. Lichten, "Precise Estimation of Tropospheric Path Delays with GPS Techniques," *The Telecommunications and Data Acquisition Progress Report 42–100, October–December 1989*, Jet Propulsion Laboratory, Pasadena, California, pp. 1–12, February 15, 1990.

[11] D. M. Tralli and S. M. Lichten, "Stochastic Estimation of Tropospheric Path Delays in Global Positioning System Geodetic Measurements," *Bull. Geod.*, vol. 64, pp. 127–159, 1990.

[12] B. L. Gary, S. J. Keihm, and M. A. Janssen, "Optimum Strategies and Performance for the Remote Sensing of Path-Delay Using Ground-Based Microwave Radiometry," *IEEE Trans. Geoscience and Remote Sensing*, vol. GE–23, no. 4, pp. 479–484, July 1985.

[13] G. M. Resch, D. E. Hogg, and P. J. Napier, "Radiometric Correction of Atmospheric Path Length Fluctuations in Interferometric Experiments," *Radio Science*, vol. 19, no. 1, pp. 411–422, January–February 1984.

[14] S. J. Keihm, *Proceedings of a Specialist Meeting on Microwave Radiometry and Remote Sensing Applications*, edited by E. R. Westwater, Boulder, Colorado, pp. 211–218, 1992.

[15] R. N. Treuhaft and G. E. Lanyi, "The Effect of the Dynamic Wet Troposphere on Radio Interferometric Measurements," *Radio Science*, vol. 22, no. 2, pp. 251–265, March–April 1987.

[16] R. P. Linfield and J. Z. Wilcox, "Radio Metric Errors Due to Mismatch and Offset Between a DSN Antenna Beam and the Beam of a Troposphere Calibration Instrument," *The Telecommunications and Data Acquisition Progress Report 42–114, April–June 1993*, Jet Propulsion Laboratory, Pasadena, California, pp. 1–9, August 15, 1993.

[17] R. F. Denning, S. L. Guidero, G. S. Parks, and B. L. Gary, "Instrument Description of the Airborne Microwave Temperature Profiler," *J. Geophys. Res.*, vol. 94, no. D14, pp. 16,757–16,765, November 30, 1989.

[18] E. R. Westwater, "Ground-Based Microwave Remote Sensing of Meteorological Variables," Chapter 4, *Atmospheric Remote Sensing by Microwave Radiometry*, edited by M. Janssen, New York: Wiley & Sons, 1993.

[19] A. E. E. Rogers, R. J. Cappallo, H. F. Hinteregger, J. I. Levine, E. F. Nes-
man, J. C. Webber, A. R. Whitney, T. A. Clark, C. Ma, J. Ryan, B. E. Corey,
C. C. Counselman, T. A. Herring, I. I. Shapiro, C. A. Knight, D. B. Shaffer,
N. R. Vandenberg, R. Lacasse, R. Mauzy, B. Rahrer, B. Schupler, and J. C. Pigg,
"Very-Long-Baseline Radio Interferometry: The Mark III System for Geodesy,
Astrometry, and Aperture Synthesis," *Science*, vol. 219, no. 4580, pp. 51–53,
January 7, 1983.

[20] C. D. Edwards, D. H. Rogstad, D. N. Fort, L. White, and B. Iijima, "The Gold-
stone Real-Time Connected Element Interferometer," *The Telecommunications
and Data Acquisition Progress Report 42-110, April–June 1992*, Jet Propulsion
Laboratory, Pasadena, California, pp. 52–62, August 15, 1992.

[21] S. T. Lowe, *Theory of Post-Block II VLBI Observable Extraction*, JPL Publica-
tion 92-7, Jet Propulsion Laboratory, Pasadena, California, 1992.

[22] E. H. Sigman, "Phase Calibration Generator," *The Telecommunications and
Data Acquisition Progress Report 42-92, October–December 1987*, Jet Propul-
sion Laboratory, Pasadena, California, pp. 89–104, February 15, 1988.

[23] M. A. Janssen, "A New Instrument for the Determination of Radio Path De-
lay Due to Atmospheric Water Vapor," *IEEE Trans. Geoscience and Remote
Sensing*, vol. GE-23, no. 4, pp. 485–490, July 1985.

[24] O. J. Sovers, *Observation Model and Parameter Partials for the JPL VLBI Pa-
rameter Estimation Software 'MODEST' — 1991*, JPL Publication 83-39, Rev. 4,
Jet Propulsion Laboratory, Pasadena, California, 1991.